# Large Eddy Simulations of flow around a circular cylinder close to a flat seabed

*Mia Abrahamsen Prsic*, Muk Chen Ong[#], Bjørnar Pettersen*, Dag Myrhaug**

* *Department of Marine Technology, Norwegian University of Science and Technology, NO-7491 Trondheim, Norway*

[#] *Department of Mechanical and Structural Engineering and Materials Science, University of Stavanger, NO-4036 Stavanger, Norway*

## *Abstract*

Large Eddy Simulations (LES) with Smagorinsky subgrid scale model are used to study the turbulent flow and wake dynamics behind a circular cylinder close to a horizontal, plane wall at subcritical Reynolds number. The focus is on investigating the details of the flow around the cylinder placed at different distances from the wall and immersed in boundary layers of various thicknesses.

The Reynolds number is Re = 13100. The simulations with gap to diameter ratios (G/D) of 0.2, 0.6 and 1 are carried out in order to investigate the changes of the flow field and the vortex shedding due to the presence of the plane wall. The influence of the incoming boundary layer profile is investigated through simulations with logarithmic boundary layer inlet profile of thickness 0.48D and 1.6D, and compared with a uniform inlet flow profile. 2D and 3D simulations are performed for Re ranging from 100 to 13100, to explore the importance of the flow three-dimensionality. The flow field in the cylinder wake, as well as the mean flow values, the spectral analysis and the pressure distribution on the cylinder surface are computed to study the flow physics due to the influences of the wall.

Keywords: LES; circular cylinder; plane wall interaction; boundary layer flow.

## 1. *Introduction*

Circular, cylindrical structures appear in many practical situations in the marine technology environment, subsea pipelines being one of them. The flow around a circular cylinder in an infinite fluid is governed by the Reynolds number ($Re = U_cD/\upsilon$, where $U_c$ is the free stream velocity, D is the cylinder diameter and $\upsilon$ is the kinematic viscosity of the fluid). The wake, whether laminar or turbulent, is symmetric and for $Re > 40$, vortices are shed periodically from the two sides of the cylinder. Proximity of the sea bottom significantly changes the flow around the pipeline and its wake. The key parameters affecting the flow, asides from Re, are the gap between the pipeline and the seabed, and the boundary layer profile of the incoming flow. In various combinations, they result in wake flow in the range from regular vortex shedding, to reattached flow with completely suppressed vortex shedding.

LES are utilized to simulate the three-dimensional (3D) flow around a circular cylinder in the vicinity of a rigid, plane wall. The simulations are made for the intermediate Re = 13100. In the North Sea, at the water depth of about 100 m, the pipelines are usually exposed to current of between 0.02 m/s and 0.5 m/s [5]. The diameter of a pipeline can vary from as much as 1.066 m (44''), through commonly used 0.76 m (30'') and 0.404 m (16'') to as small as 0.05 m (2'') [6]. The chosen Re thus covers a variety of combinations of operational conditions for subsea pipelines.

Several detailed experimental studies were carried out at subcritical $Re = O(10^4)$. In this Re range, the vortex shedding is relatively insensitive to Re variation, allowing data comparison for studies conducted at slightly different Re. Particle Image Velocimetry (PIV) measurements were performed in [7] for Re between 1200 and 4960; [8] for Re = 840, 4150 and 9500. [9] measured the flow features for Re = 12000. Point measurements of pressure and velocity in the flow fields for comparable Re are presented at [10], [11] and [12].

LES have proven to be a successful model for detailed simulations of the flow around a circular cylinder in an infinite fluid and uniform inflow in the subcritical flow regime. Breuer [1] presented an extensive analysis of the influence of the subgrid scale models, the grid resolution and the discretization schemes on the quality of the LES results. Tremblay et al. [2] carried out a series of LES and compared them with the results from Direct Numerical Simulations (DNS). Parnaudeau et al. [3] focused on the comparison of their LES results of the near wake flow with the experimental results obtained by PIV. Abrahamsen Prsic et al. [4] investigated the influence of the numerical parameters on LES and discussed the details of the near wake flow for the same Re as chosen in this study.

For the cylinder in the vicinity of a wall, several researchers performed two-dimensional (2D) simulations using Reynolds – Averaged Navier–Stokes (RANS) models. At a comparable Re, [13] and [14] performed the simulations with URANS k-ε model. Even though the model provided a good qualitative agreement with the experimental results, RANS showed significant limitations. Modelling of the intrinsically 3D flow with 2D simulations led to the under-prediction of the drag and the lift forces. A three-dimensional LES model is therefore utilized in the present study. LES were also used to simulate the flow around a square cylinder in the vicinity of a plane wall, at a comparable Re = 22000; [16] and [17] provided promising results and good comparison to the experimental research. Based on these references, LES are considered to be an appropriate tool for performing the simulations of the flow around a circular cylinder in the vicinity of a plane wall at intermediate Re.

## *2. Numerical method*

### 2.1. Governing equations

In the present study, the incompressible Navier-Stokes equations are solved by LES. In the filtered form, the continuity and the momentum equations can be written:

$$\frac{\partial \overline{u}_i}{\partial x_i} = 0 \tag{1}$$

$$\frac{\partial \overline{u}_i}{\partial t} + \frac{\partial \left( \overline{u}_i \overline{u}_j \right)}{\partial x_j} = -\frac{1}{\rho} \frac{\partial \overline{p}}{\partial x_i} + \nu \frac{\partial^2 \overline{u}_i}{\partial x_j{}^2} - \frac{\partial \tau_{ij}}{\partial x_j} \tag{2}$$

where $u_i$ , i = 1, 2, 3 denotes the filtered velocity component in streamwise ($x$), crossflow ($y$) and spanwise ($z$) direction respectively ($x_i$ is assigned to the respective directions), $\rho$ is the density of the fluid and $p$ is the filtered pressure. $\tau_{ij}$ represents the non-resolvable subgrid stress, given by:

$$\tau_{ij} = \overline{u_i u_j} - \overline{u}_i \overline{u}_j \tag{3}$$

Here, $\tau_{ij}$ describes the influence of the small scale structures on the large eddies. LES is in detail presented in [20]. The subgrid scale motions are modelled by a commonly used Smagorinsky model proposed in [18]. It assumes that the eddy viscosity is proportional to the subgrid scale characteristic length and to the characteristic subgrid scale velocity. The Smagorinsky constant is fixed; $C_s$ = 0.2 in the present study. Several studies compared the performance of various LES subgrid scale models for the case of a cylinder in an unlimited fluid at Re = 3900. [1], [2], [15] and [19] showed that the standard Smagorinsky model performs well in comparison to the more complex subgrid scale models for the type of flow similar to the present study.

All the simulations are performed using the open source code OpenFOAM. The PISO algorithm (Pressure Implicit with Splitting of Operators, see [20]) is used to solve the Navier-Stokes equations. For the time integration, an implicit, backward differencing method of second order is used. Spatial schemes for the gradient terms are Gauss linear and Gauss limited linear. All of the above schemes are of second order accuracy, most commonly used in engineering applications of LES, [21]. Discussion of the influences of the various numerical parameters can be found in [1], confirming the validity of the choice of central differencing schemes for the convective terms.

## 2.2. Computational setup

The LES are performed on a 3D rectangular computational domain extending from 10D in front of the cylinder to 30D in the wake. In the crossflow direction, it extends from the rigid wall at G clearance to 10D above the cylinder centre (Figure 1). The spanwise length of the domain is 4D (and 8D for one case). The chosen domain is larger than the domains successfully used in several studies of the flow with comparable and higher Re, amongst others [4], [22] and [23]. It is therefore believed that the domain boundaries have negligible influence on the flow close to the pipeline in the present study. Detailed discussion of the domain sizes is given in [4].

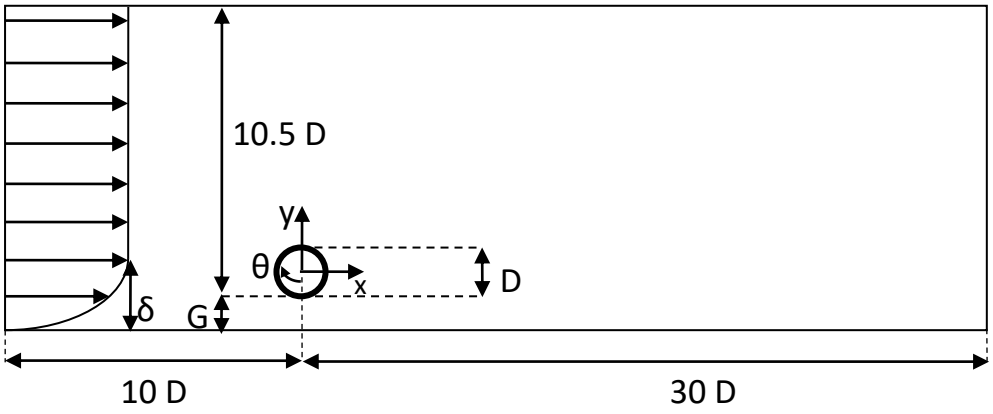


Figure 1. Definition sketch for the cylinder in the vicinity of a plane wall. Coordinate system origin is in the centre of the cylinder, z/D = [0, 4]. In the present study, G/D = 0.2, 0.6 and 1; δ/D = 0, 0.48 and 1.6.

A body-fitted, structured O-mesh is used. The details of the mesh are presented in Figure 2. In all simulations, the size of the elements near the cylinder and the horizontal bottom wall is chosen such that the maximum dimensionless wall distance $\eta^+$ is kept below 1. Here $\eta^+$ is defined as $\eta^+ = u_* \eta'/\nu$, where $u_*$ denotes the friction velocity near the wall, and $\eta'$ is the normal distance from the wall. Detailed grid convergence studies are presented in Section 3.2.

The boundary conditions are kept the same through the entire study. A boundary layer flow is specified by imposing a logarithmic profile at the inlet. Several boundary layer thicknesses are used (see Table 1 and 3). The incoming free stream velocity outside the boundary layer is constant. At the outlet, the pressure and the normal gradient of the velocity are set to zero. The upper boundary is defined as a symmetry boundary condition. The boundaries normal to the cylinder axis have the periodic boundary conditions, while the no-slip condition is applied on the fixed cylinder surface and the bottom wall.

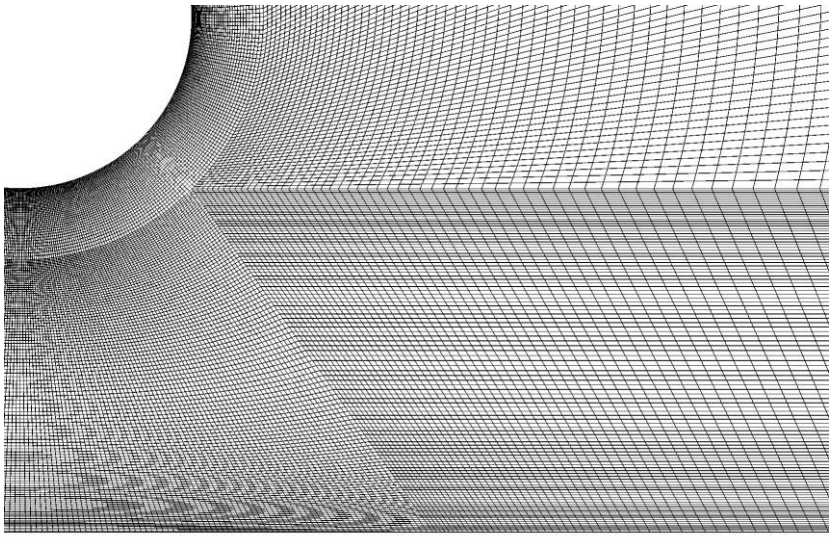

Figure 2. Details of the mesh in the vicinity of the cylinder, the wall and in the near wake region. G/D = 1.

## *3. Code validation and convergence studies*

### 3.1. Cylinder in an infinite fluid at Re = 13100 – code validation

The OpenFOAM LES code is validated through a simpler and thoroughly investigated case – the flow around a circular cylinder in an infinite fluid, subjected to a uniform inflow. The validation was performed in [4] for the benchmark case of Re = 3900 and a higher Re = 13100 case. Details of the simulations, the convergence studies and the thorough analysis of the results are presented in [4]. The code is validated by comparing the LES results to numerical and experimental results available. The results are analysed through the time- and spanwise-averaged drag and lift coefficients, the velocity profiles in the cylinder wake, the mean recirculation length ($L_r$) and the time-averaged streamlines in the cylinder wake. The results, in details discussed in [4], compare well to the previously published research. It is thus confirmed that LES with the Smagorinsky model, performed by using the OpenFOAM code, are suitable for simulating the flow in the subcritical flow regime.

## 3.2. Cylinder in the vicinity of a wall - convergence studies

To mimic a fully developed boundary layer profile that free spanning pipelines close to the seabed encounter in the natural environment, the inlet flow is simulated with a logarithmic profile in the vicinity of the wall. Vertically dependant streamwise velocity u(y) is defined as:

$$u(y) = \min\left\{\frac{u_*}{\kappa}\ln\left(\frac{y}{z_w}\right), U_c\right\} \quad (4)$$

$$u_* = \frac{\kappa U_c}{\ln(\delta / z_w)} \quad (5)$$

Here $U_c$ is the free stream velocity, $\kappa = 0.41$ is the von Karman constant, $z_w = 1 \times 10^{-6}$m is the seabed roughness, and $\delta$ is the dimensional boundary layer thickness. The dimensionless boundary layer thickness ($\delta/D = 1.6$ and 0.48) is imposed on the domain inlet, 10D upstream from the cylinder. To check the behaviour of the profile when it approaches the cylinder, the following simulation is performed. Keeping the same domain size, the cylinder is removed and an orthogonal mesh is created with the same resolution in the vicinity of the wall (see Table 1 – boundary layer). The streamwise velocity is averaged in time for the fully developed flow and sampled on several vertical cross-sections between the inlet and the position of the cylinder, indicated in Figure 3a. Comparison of the velocity profiles at these cross-sections (Figure 3b) shows only negligible changes of the profile along the wall in front of the cylinder. This leads to the conclusion that the cylinder is exposed to a fully developed boundary layer profile with the chosen $\delta/D$.

The flow around the cylinder in the vicinity of a wall is divided into two distinctive categories – the narrow and the wide gap flow. Due to the intrinsic differences in the flow behaviour, a grid convergence study is performed for both flow regimes. $G/D = 0.2$ and 0.6 represent the narrow and the wide gap flow regime, respectively. The boundary layer thickness, $\delta/D = 1.6$, is kept the same in both cases. Following the ASME Standard for Verification and Validation [24], three meshes are created for each grid study. The size of the elements at the cylinder and the bottom wall surface is kept constant for these simulations. In the grid refinement sequence, the grid cells are geometrically similar, with constant refinement factor in all directions, [24]. The elements in the gap and close to the cylinder maintain the same shape and overall distribution. Details about the cases can be found in Table 1 - mesh.

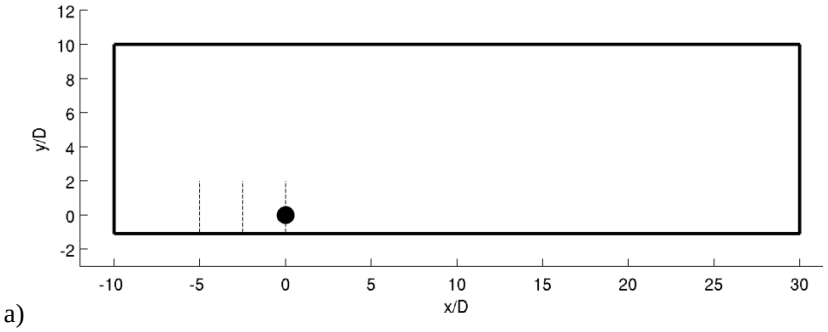


a)

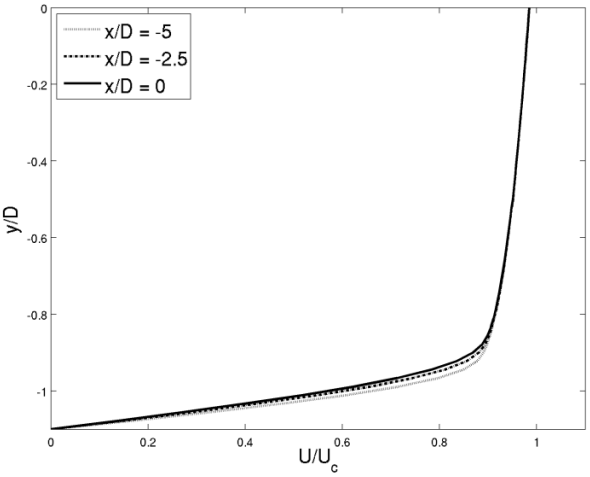


b)

Figure 3. a) Schematic representation of the computational domain slice in (x, y) plane, z/D = 2. Positions of the velocity sampling cross-sections are indicated with dotted lines. b) time-averaged and normalized streamwise velocity component ($U/U_c$) profile at three cross-sections. δ/D = 1.6, case wall00.

TABLE 1: Numerical set-up for all convergence study cases. δ/D = 1.6.

| Case | Key parameter | Re | G/D | Computational domain (x D) | Total number of elements (million) | Number of elements circumf. | Time-step Δt (s) |
|---|---|---|---|---|---|---|---|
| G06 m1 | Mesh | 13100 | 0.6 | 40 x 11.1 x | 7.5 | 360 | 0.0001 |
| G06 1 | Gap | 13100 | 0.6 | 40 x 11.1 x 4 | 9.5 | 410 | 0.0001 |
| G06 m2 | Mesh | 13100 | 0.6 | 40 x 11.1 x 4 | 12.5 | 440 | 0.0001 |
| G06 t1 | Time-step | 13100 | 0.6 | 40 x 11.1 x 4 | 9.5 | 410 | 0.00025 |
| G06 t2 | Time-step | 13100 | 0.6 | 40 x 11.1 x 4 | 9.5 | 410 | 0.0005 |
| 2D Re100 | 3D effects | 100 | 0.6 | 40 x 11.1 (2D) | 0.02 | 200 | 0.0001 |
| Re100 4D | 3D effects | 100 | 0.6 | 40 x 11.1 x 4 | 2 | 200 | 0.0001 |
| 2D Re500 | 3D effects | 500 | 0.6 | 40 x 11.1 (2D) | 0.023 | 215 | 0.0001 |
| Re500 4D | 3D effects | 500 | 0.6 | 40 x 11.1 x 4 | 2.3 | 215 | 0.0001 |
| 2D Re1000 | 3D effects | 1000 | 0.6 | 40 x 11.1 (2D) | 0.5 | 320 | 0.0001 |
| Re1000 4D | 3D effects | 1000 | 0.6 | 40 x 11.1 x 4 | 5 | 320 | 0.0001 |
| 2D Re3900 | 3D effects | 3900 | 0.6 | 40 x 11.1 (2D) | 0.75 | 360 | 0.0001 |
| Re3900 4D | 3D effects | 3900 | 0.6 | 40 x 11.1 x 4 | 7.5 | 360 | 0.0001 |
| 2D Re7800 | 3D effects | 7800 | 0.6 | 40 x 11.1 (2D) | 0.75 | 360 | 0.0001 |
| Re7800 4D | 3D effects | 7800 | 0.6 | 40 x 11.1 x 4 | 7.5 | 360 | 0.0001 |
| G06 L8 | Spanwise length | 13100 | 0.6 | 40 x 11.1 x 8 | 19 | 410 | 0.0001 |
| G02 m1 | Mesh | 13100 | 0.2 | 40 x 10.6 x 4 | 5.2 | 360 | 0.0001 |
| G02 m2 | Mesh | 13100 | 0.2 | 40 x 10.6 x 4 | 7.2 | 410 | 0.0001 |
| G02 1 | Gap | 13100 | 0.2 | 40 x 10.6 x 4 | 9.5 | 460 | 0.0001 |
| wall00 | Boundary layer | 13100 | No cyl. | 40 x 11.1 x 4 | 7.2 | No cylinder | 0.0001 |

The influence of the mesh and the time-step is first analysed through the time- and spanwise-averaged (mean) drag coefficient ( $\overline{C_d}$ ), the mean lift coefficient ( $\overline{C_l}$ ), the root-mean-square of the lift coefficient ($C_{lrms}$) and the Strouhal number (St), see Table 2. The aforementioned drag ($C_d$) and lift ($C_l$) coefficients are defined as: $C_d = F_d/(0.5\rho U_c^2 A)$ where $F_d$ is the drag force exerted on the entire cylinder, and A is the projected area of the cylinder; $C_l = F_l/(0.5\rho U_c^2 A)$, where $F_l$ is the integrated lift force. The Strouhal number is defined as $St = f\, D/U_c$, where f is the vortex shedding frequency.

TABLE 2: Mean flow parameters for all convergence study cases. G/D = 0.2 and 0.6; δ/D = 1.6.

| Case | Key parameter | $\overline{C_d}$ | $\overline{C_l}$ | $C_{lrms}$ | St |
|---|---|---|---|---|---|
| G06 m1 | Mesh | 1.061 | 0.070 | 0.106 | 0.273 |
| G06 1 | Gap | 1.060 | 0.083 | 0.115 | 0.278 |
| G06 m2 | Mesh | 1.049 | 0.083 | 0.099 | 0.287 |
| G06 t1 | Time-step | 1.099 | 0.092 | 0.171 | 0.253 |
| G06 t2 | Time-step | 1.109 | 0.081 | 0.179 | 0.259 |
| Re100 0D | 3D effects | 1.257 | 0.049 | 0.049 | |
| Re100 4D | 3D effects | 1.256 | 0.049 | 0.049 | |
| Re500 0D | 3D effects | 1.299 | 0.040 | 0.676 | |
| Re500 4D | 3D effects | 1.296 | 0.038 | 0.685 | |
| Re1000 0D | 3D effects | 1.321 | 0.019 | 0.883 | |
| Re1000 4D | 3D effects | 1.139 | 0.050 | 0.366 | |
| Re3900 0D | 3D effects | 1.629 | 0.253 | 1.320 | |
| Re3900 4D | 3D effects | 1.221 | 0.043 | 0.385 | |
| Re7800 0D | 3D effects | 1.657 | 0.183 | 1.383 | |
| Re7800 4D | 3D effects | 1.087 | 0.079 | 0.138 | |
| G06 L0 | Spanwise length | 1.695 | 0.123 | 1.400 | |
| G06 L8 | Spanwise length | 1.080 | 0.091 | 0.126 | 0.271 |
| G02 m1 | Mesh | 0.885 | 0.040 | 0.041 | - |
| G02 m2 | Mesh | 0.887 | 0.043 | 0.043 | - |
| G02 1 | Gap | 0.889 | 0.045 | 0.044 | - |

At G/D = 0.6, the results for different meshes (see Table 2) suggest that convergence is achieved. The mesh refinement leads to a slight decrease in $\overline{C_d}$ , but the difference in the values between the finest and the coarsest mesh is only 1.1%. $\overline{C_l}$ increases 15% between the cases with the coarsest and the intermediate mesh, while further mesh refinement leads to a decrease of only 0.6%. The variations in $C_{lrms}$ are less than 7% from the finest to the coarsest mesh. St increases 2% between the coarse and the intermediate mesh and 3% for the further refinement. These results suggest that the mesh with 9.5 million elements (case G06 1) provides sufficient refinement.

The grid convergence study for G/D = 0.2 is shown in Table 2. $\overline{C_d}$ varies only 0.5% between the cases with the coarse and the fine mesh. The mesh refinement from 5.2 to 7.2 million elements leads to 7.7% increase in $\overline{C_l}$ and 6% increase in $C_{lrms}$. Further mesh refinement to 9.5 million

elements results in 4.8% increase of $\overline{C_l}$ and 2.5% of $C_{lrms}$. Since there is no periodic oscillations due to cease of vortex shedding, St is not investigated. These results suggest that the finest mesh (G02 1 case) is fine enough for the further analysis.

The velocity field is analysed over several vertical cross-sections (y, z plane). They are positioned from x/D = 0 (at the centre of the cylinder) to 8.5, with more focus on the near wake. The mean streamwise velocity (U) is sampled at several cross-sections distributed evenly along the cylinder span (z-axis direction) and spanwise-averaged for each x/D. Such mean velocity profiles for G/D = 0.6 are presented in Figure 4a. Close to the cylinder, simulations with all three meshes yield profiles with no significant differences. Due to the mesh stretching, slight discrepancies develop for $x/D \geq 1.5$. The differences between all three cases are, however, small along the cylinder wake. Very similar behaviour is observed for G/D = 0.2, presented in Figure 4b. Combined with the results of the mean flow values, this leads to the conclusion that cases G06 1 and G02 1 have sufficient grid resolution to resolve the details of the flow.

The grid convergence study is not carried out for the third case of interest, i.e. for G/D = 1 in order to avoid unnecessary high computational cost. The flow at G/D = 1 belongs to the wide gap regime, the same as for G/D = 0.6. The sensitive interaction between the cylinder and the wall boundary layer subsides at large gaps, and the flow resembles the one around a cylinder in an infinite fluid, [7]. Therefore, both the previous experience of simulations with a cylinder in an infinite fluid at the same Re, [4], and the convergence study for the present G/D = 0.6 case, are utilized to create the mesh for G/D = 1. A total of 9.8 million elements is distributed in the same manner as in the G06 1 case. The element size at the bottom wall and at the cylinder surface is kept the same as in all the previous cases, and additional elements are added in the gap between the cylinder and the wall.

Results for the convergence study of the time-step ($\Delta t$) are presented in Table 2. It can be concluded that the refinement of the time-step does not lead to significant changes in St or the integrated forces on the cylinder. $\overline{C_d}$ varies less than 5% between the smallest and the largest time-step, $\overline{C_l}$ is changing about 10%, and St increases by 6% between the largest and the smallest time-step.

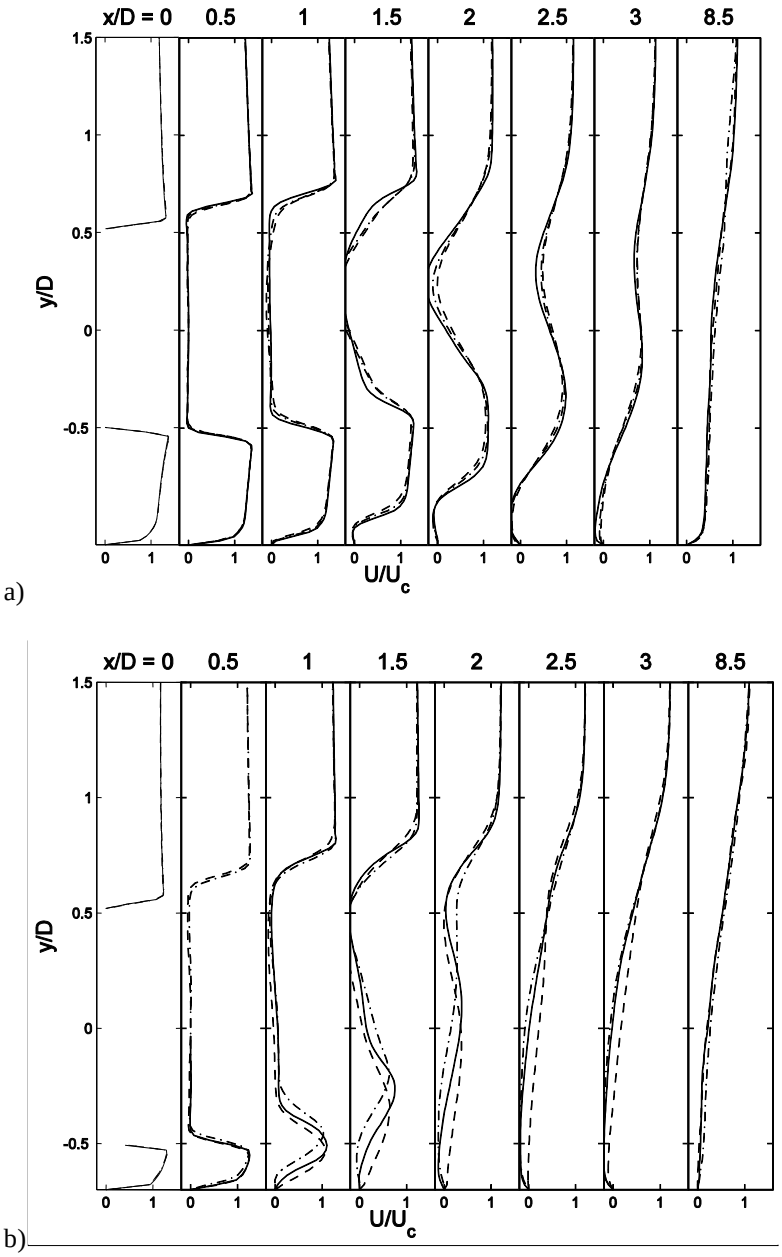


Figure 4. $U/U_c$ across vertical cross-sections in the (y, z) plane of the cylinder wake. Grid convergence study.
a) G/D = 0.6, symbols: -·- G06 m1 (coarse), - - G06 1, — G06 m2 (fine);
b) G/D = 0.2, -·- G02 m1 (coarse), - - G02 m2, — G02 1 (fine).

The influence of the time-step is further investigated through the velocity profiles in the cylinder wake. The velocity field is sampled in the (x, z) plane, and averaged in the spanwise direction. Figure 5 shows that the differences between the cases are small. It is therefore concluded that a time-step of 0.0001s is sufficient for the further analysis. Based on the current results and the previous experience published in [4], the results are not showing high sensitivity on the choice of time step. Therefore, we conclude that the time-step used in the G06 1 case is also fine enough for the cases with G/D = 0.2 and 1.

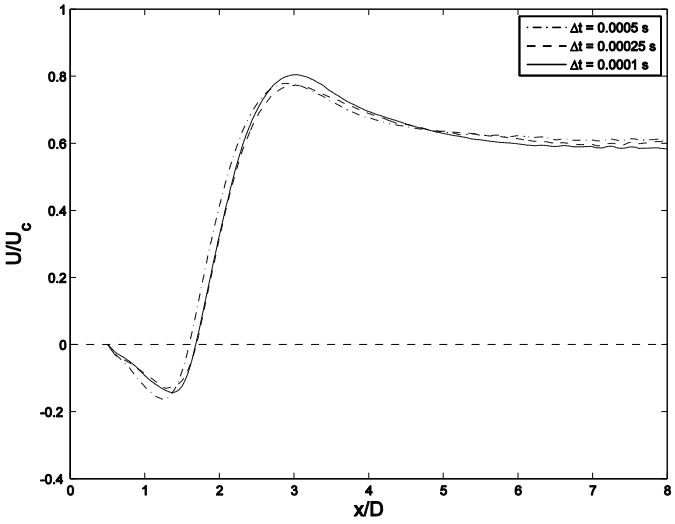


Figure 5. $U/U_c$ in the cylinder wake, in the (x, z) plane, y/D = 0 versus the time-step. G/D = 0.6, δ/D = 1.6.

Another computational parameter of importance for the 3D simulations is the spanwise (z) width of the computational domain. For the case of the cylinder in an infinite fluid, the wake in the subcritical regime is varying along the cylinder span [25]. It forms cells, leading to the variations of the forces exerted on the cylinder. For a smooth cylinder with Re between 11000 and 45000, the cell length is measured to be between 3D and 6D, [25]. [26] conducted experiments at Re = 19000 (comparable to the present study) and found the cell length to be approximately 3D, indicating the minimum domain width for the numerical simulations.

However, most of the previously performed numerical simulations of the flow in the vicinity of a plane wall were made with 2D models, see e.g. [22], [23]. In order to check the importance of the 3D effects at various Re, several simulations are performed with both two- and the three-dimensional domains. The simulations are performed at Re = 100, 500, 1000, 3900, 7800 and 13100 for G/D = 0.6, using the same computational parameters and the criteria for the numerical mesh as described in Section 2. Details of the simulations are presented in Table 1.

For both Re = 100 and 500, $\overline{C_d}$ and $C_{lrms}$ of the 2D and 3D simulations differ with less than 1%, see Figure 6. This is in good agreement with the nature of the wake flow for such low Re, where Re < 300 represents the laminar wake regime and Re = 500 belongs to the very low subcritical regime, with negligible spanwise variability in both cases, see [25]. The 2D simulations, however, are shown not to be suitable for the flow at higher Re (Re ≥ 1000), where the flow is turbulent and 3D. While the 3D simulations capture decreasing $\overline{C_d}$ for increasing Re, $\overline{C_d}$ obtained by the 2D simulations increase with increasing Re (see Figure 6a), progressively deviating from the 3D results. While the attenuation of the lift oscillations due to the presence of the wall is captured by the 3D simulations, the 2D cases give very high $C_{lrms}$ at high Re (Figure 6b). For Re =13100 (the highest in this study) the 3D

simulations yield $\overline{C_d}$ = 1.059 and $C_{lrms}$ = 0.115, which are in good agreement with the previously published numerical and experimental results (see Section 4.1). However, $\overline{C_d}$ = 1.695 and $C_{lrms}$ = 1.408 for the 2D simulations do not agree with the previous results. It is thus concluded that the 3D effects are crucial for the turbulent flow around the cylinder in the vicinity of the wall. 3D simulations also allow the analysis of the flow through the spatial distributions of the velocity and pressure fields, making them more comparable to the experimental studies (which are intrinsically 3D).

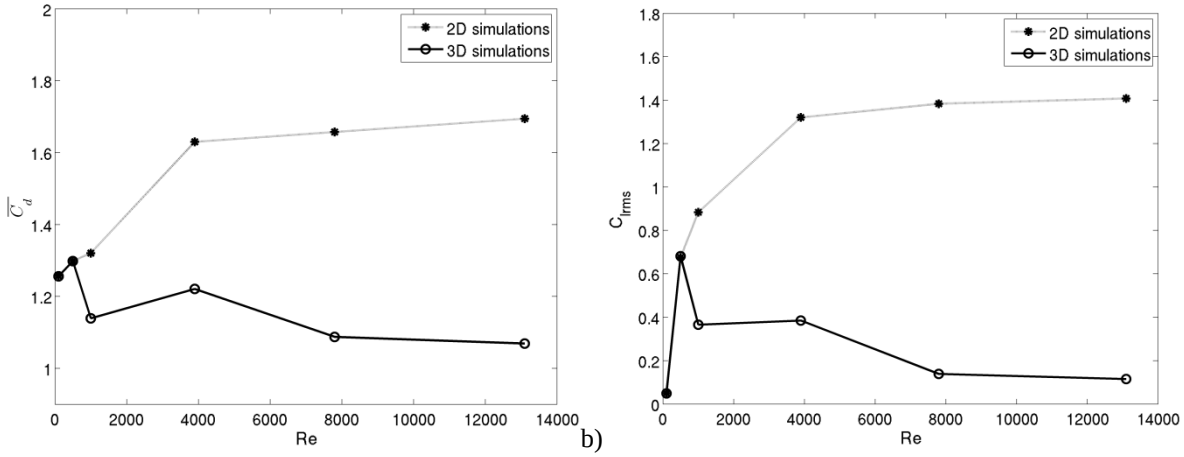


a) b)

Figure 6. $\overline{C_d}$ and $C_{l\,rms}$ versus Re – a comparison of 2D and 3D simulations.

By using a 3D LES, similar flow was successfully modelled in [27] with a three diameter wide domain in spanwise direction. The study was, however, done for the lower Re of 1400. Due to the limited numerical studies of this problem, the present domain width is chosen with reference to the previously published work for the case of the cylinder in an infinite fluid with same Re, [4]. In [4], the domain extended over 4D spanwise. For a comparable Re, [28] used a domain of 4D spanwise width, while a πD wide domain was used by [2], [3] and [19]. Thus the domain spanning over 4D is chosen here.

To check how well the spanwise structures are captured in the present case, the simulations were performed for 4D and 8D domain widths. The other numerical parameters are kept the same as for the converged case for G/D = 0.6, see Table 1. The visualization of the flow is done through the Q-criterion, a tool capable of depicting the coherent spanwise structures, [29]. In the 4D wide domain, cells of 3-4D length can be clearly detected (Figure 7a). This type of structures, of approximately same length, shows up also in the wider domain case, repeating twice over the cylinder span (Figure 7b). The flow around the cylinder in an infinite fluid [4] and in the vicinity of the wall show similar behaviour in the spanwise direction. Since the cells in both cases are approximately 3D long, the domain of 4D spanwise length is considered to be sufficient.

The time-averaged values, such as mean drag and lift coefficients are confirming the previous conclusion. $\overline{C_d}$ differs for less than 2% between the 4D and the 8D cases, and St is almost identical

for both cases. The lift coefficient also shows good resemblance in both mean and RMS values. It is therefore concluded that the spanwise length of 4D is wide enough for capturing the three-dimensional effects.

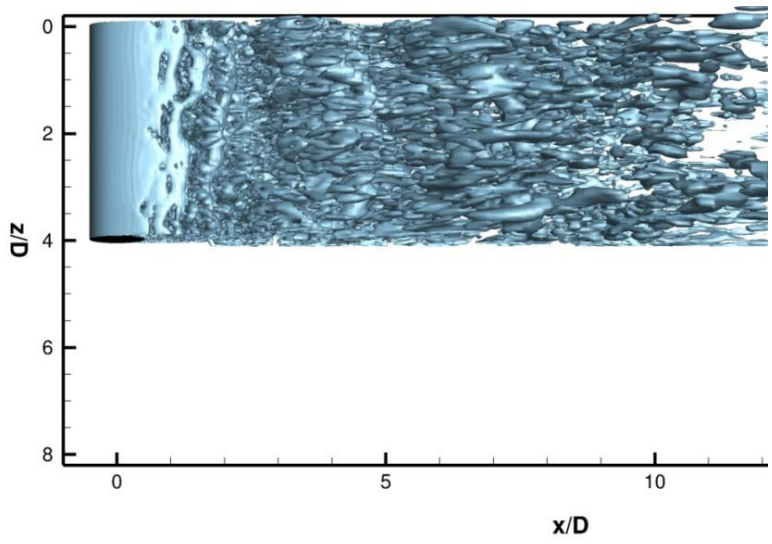


a)

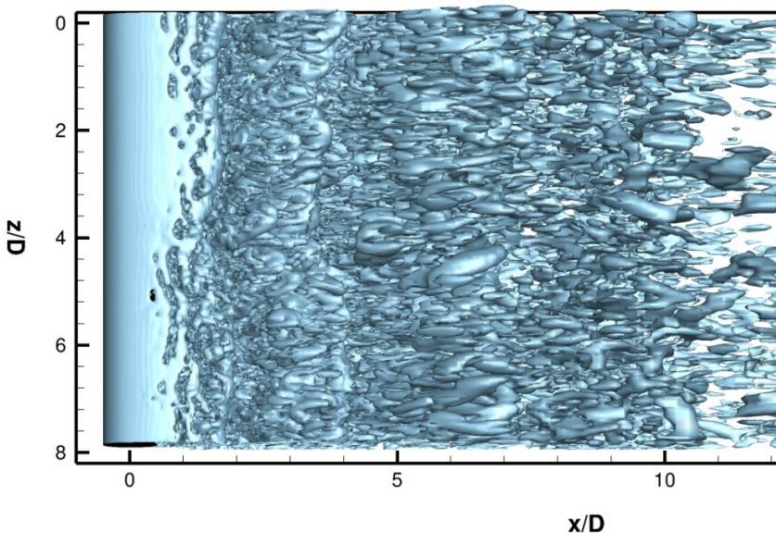


b)

Figure 7. Examples of the instantaneous Q = 1 iso-surfaces for the cylinders of different spanwise lengths. G/D = 0.6, δ/D = 1.6. a) L/D = 4, case G06 1; b) L/D =8, case G06 L8. (Point of view is from above the cylinders.)

## *4. Results for the cylinder in the vicinity of a plane wall at Re = 13100*

The effect of G/D on the forces exerted on the cylinder, and the properties of the flow in the wake, are explored by choosing G/D = 0.2, 0.6 and 1 (see Table 3). G/D = 0.2 and 1 are chosen within the typical values for the narrow and the wide gap flow regime, while G/D = 0.6 approaches the transient regime, [30]. In this way, the main types of flow around the cylinder in the vicinity of a plane wall are addressed.

The influence of δ/D is investigated by choosing the values δ/D = 0, 0.48 and 1.6, see Table 3. Here, δ/D = 0 corresponds to a uniform inlet velocity profile which, when approaching the cylinder, develops into a thin boundary layer with δ/D < 0.2D. These δ/D values are chosen to mimic the conditions at the seabed - a very thin boundary layer, the fully developed one, and a thick boundary layer caused by, for example, a bluff body obstacle, [11].

TABLE 3: Numerical set-up. Cylinder close to the wall at various G/D and δ/D. $\Delta t = 0.0001$.

| Case | G/D | δ/D | Computational domain (x D) | Total number of elements (million) |
|---|---|---|---|---|
| G02 1 | 0.2 | 1.6 | 40 x 10.7 x 4 | 9.0 |
| G06 1 | 0.6 | 1.6 | 40 x 11.1 x 4 | 9.5 |
| G1 1 | 1 | 1.6 | 40 x 11.5 x 4 | 9.8 |
| G06 i1 | 0.6 | 0 | 40 x 11.1 x 4 | 9.5 |
| G06 i2 | 0.6 | 0.48 | 40 x 11.1 x 4 | 9.5 |

### 4.1. Influence of the gap (G/D)

Figure 8, presenting $\overline{C_d}$ and $C_{lrms}$ for various G/D, agrees with both experimental and numerical results that recorded a decrease in $\overline{C_d}$ as G/D narrows ([30]; [27]). [30] summarized that the wall proximity maintains its strong influence for small G/D ratios, leading to the complete disappearance of vortex shedding for the narrowest gaps. As G/D exceeds 1, this influence becomes insignificant and thus the flow behaves similar to the case of a cylinder in an infinite fluid.

TABLE 4: Cylinder close to the wall at various G/D and δ/D. Mean flow parameters.

| Key parameter | Case | $\overline{C_d}$ | $\overline{C_l}$ | $C_{lrms}$ | St |
|---|---|---|---|---|---|
| G/D | G02 1 | 0.889 | 0.045 | 0.044 | - |
| G/D | G06 1 | 1.060 | 0.083 | 0.115 | 0.278 |
| G/D | G1 1 | 1.441 | 0.060 | 0.710 | 0.219 |
| δ/D | G06 i1 | 1.437 | 0.135 | 0.614 | 0.234 |
| δ/D | G06 i2 | 1.161 | 0.118 | 0.163 | 0.275 |

In Table 4 and Figure 8, the results are compared to the measurements of [11] who reported $\overline{C_d}$ = 0.9 at G/D = 0.2, $\overline{C_d}$ = 1.36 at G/D = 0.6 and $\overline{C_d}$ = 1.42 at G/D = 1. Comparison of the results for the narrow and the wide gap show very good agreement, within 5%. The differences in the G/D = 0.6 case might be attributed to the different structures of the boundary layers. To obtain the boundary layer thickness of 1.64D, [11] used rod-generated boundary layer. There, the velocity gradient closer to the wall was larger than in the naturally developed logarithmic profile. In [11], the variation of the mean drag coefficients showed sensitivity on the boundary layer structure. This influence can also be seen in the results for the widest gap, G/D = 1. For the case of a thinner, but naturally developed boundary layer, Lei et al. [11] measured $\overline{C_d}$ = 1.43, very close to the present $\overline{C_d}$ = 1.44. On the other hand, $\overline{C_d}$ = 1.32 from the rod-generated boundary layer agrees very well with $\overline{C_d}$ = 1.31 for the present study of the cylinder in the unbounded flow (Figure 8a). A very similar effect can be noticed on $C_{lrms}$ in Figure 8b. Results for the small gap are again in good agreement while the widest gap results in [11] compare very well to the $C_{lrms}$ values for the cylinder in an infinite fluid [4].

Zdravkovich [31] performed a series of experiments varying G/D in the wind tunnel, at Re = 61000. As presented in Figure 8a, the results show a similar trend as present, but with significantly lower values. According to [31], the measured drag coefficient was lower "presumably due to the small aspect ratio of the cylinders" used in the experiments.

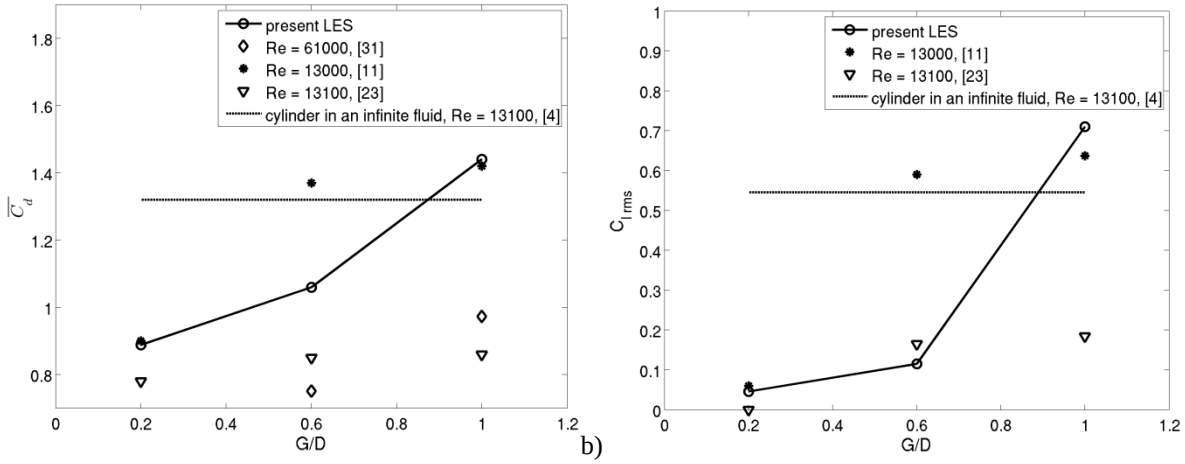


a) b)

Figure 8. $\overline{C_d}$ and $C_{l\,rms}$ versus G/D.

By comparing the present results to the previous ones from the numerical simulations, the significance of the 3D LES simulations becomes clear. The decrease in $\overline{C_d}$ with the narrowing of the gap is almost completely absent in 2D RANS simulations with a k-ε model, [23], for the same Re (Figure 8a). At G/D = 0.2, the 2D and 3D results show reasonable agreement. Increasing the gap, $\overline{C_d}$

in the 2D simulations remains low, 20% lower than the LES results at G/D = 0.6 and 38% lower for G/D = 1. [32] faced similar shortcomings, using a k-ω model and Re = 9000. On the other hand, [27] performed LES for G/D = 0.2 and 1, for a lower Re = 1440. The flow at Re = 1440 falls between two regimes, TRSL1 (Transition in shear layers – development of transition waves) and TRSL2 (Transition in shear layers – formation of transition eddies), while Re = 13100 belongs to the latter one, [33]. Both Re, however, belong to the subcritical flow regime, with a fully turbulent wake and a laminar boundary layer separation, [25]. The results are in very good agreement with the present study.

$C_{lrms}$ is a good indicator of the changes in the flow amplitude and regularity. Vortex shedding is significantly suppressed for G/D < 0.3, [30]. This is confirmed in the present study through a very low $C_{lrms}$ at G/D = 0.2. The present $C_{lrms}$ results are compared to the 2D RANS results by [23]. For G/D = 0.2, both models predict suppression of the regular vortex shedding. However, due to the very fine mesh resolution in the vicinity of the cylinder, LES are capturing the small $C_l$ variations where the coarser RANS model does not capture any fluctuations at all ($C_{lrms}$ = 0, [23]). The results of the two models are in reasonable agreement for G/D = 0.6, while the largest discrepancies emerge at G/D = 1 ([23] report $C_{lrms}$ at only 25% of the present value). The 2D simulations do not capture the strong increase in $C_{lrms}$ value at the larger gaps, confirmed by both the experiments and the present 3D simulations.

In agreement with [11], the fluctuations of the lift coefficient at G/D = 0.2 confirm the existence of weak oscillations in the cylinder wake. The vortex shedding is, however, suppressed making the discussion of the Strouhal number for the smallest gap redundant. On the other hand, for G/D > 1, [30] expected that the St is unaffected by the presence of the wall (St ≈ 0.21). This compares well to the present study where St = 0.219 for G/D = 1. In the wide gap regime, experimental results by [7], [9] and [11], as well as the numerical results of [23] and [27], show very good agreement with this study. For the narrower gaps, the St discrepancy is large. PIV measurements by [7] for Re = 4900 and LES by [27] for low Re = 1440 captured a decrease of St with increasing gap, similar to the present study. [11] also noticed an increase in the St for transient G/D around 0.5, however, with St < 0.2 for any gap. On the other hand, for Re = 12000, [9] noticed almost no variation of St for G/D between 0.1 and 2, while [23] reported an increasing St with increasing G/D. To explore the origin of the discrepancy, the influence of the δ/D ratio is discussed in Section 4.2.

Physical behaviour of the flow can be further explored by analysing the velocity profiles in the cylinder wake. The mean velocity profiles for all three G/D ratios are presented in Figure 9a. Within the first 0.5D downstream from the cylinder centre, the flow behaviour is similar for all gaps. At x/D = 1, the profiles for the two wider gaps are nearly symmetric around the cylinder axis. The noticeable difference occurs in the area directly overshadowed by the cylinder (y/D between -0.5 and 0.5). For G/D = 0.6, the velocities are still very low at the height of the cylinder, forming an 'u-profile' (see

[15]) and pointing towards an elongated wake. On the other hand, the velocity profile for G/D = 1 already resembles the classical 'v-profile' of the cylinder in an infinite fluid.

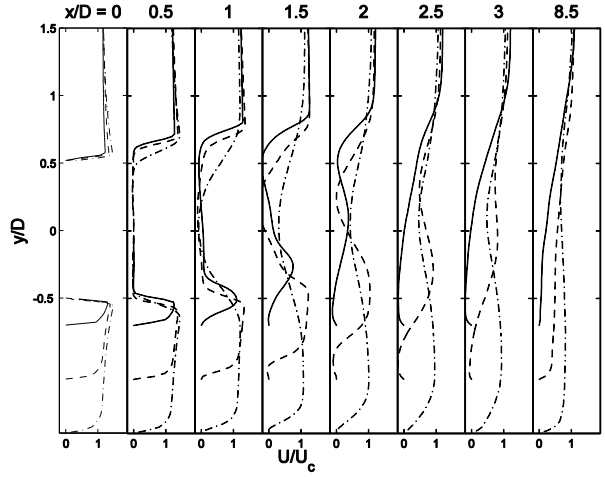


a)

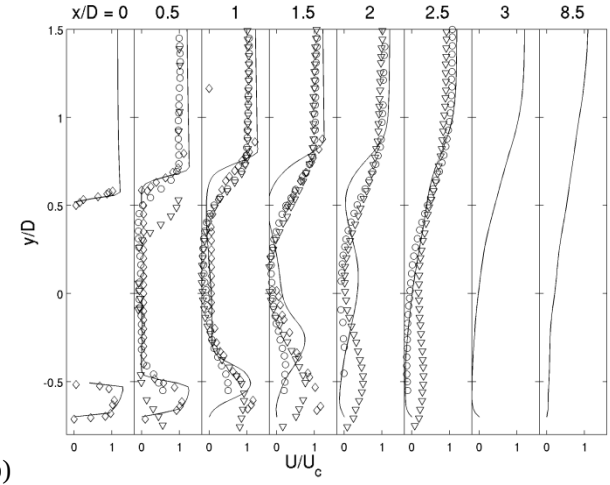


b)

Figure 9. $U/U_c$ profile in the cylinder wake, in the (y, z) plane.
a) — G/D = 0.2, - - G/D = 0.6, -·- G/D = 1 (present).
b) — G/D = 0.2 (present);
o G/D = 0.1, δ/D = 0.4, Re = 1.2 x $10^4$, Wang and Tan [9]; ◊ G/D = 0.2, δ/D = 1.4, Re = 0.95 x $10^4$, Alper Oner et al. [8]; ∇ G/D = 0.3, δ/D = 0.4, Re = 1.2 x $10^4$, Wang and Tan [9].

Farther downstream in the wake, the velocity profiles for G/D = 1 retain symmetry. This behaviour is documented in previous studies, [8], [9]. The bottom boundary layer eventually assumes its original shape, while the velocities in the area overshadowed by the cylinder continue to form the 'v-profile' far back in the wake. At G/D = 0.6, the velocities at -0.5 < y/D < 0.5 develop the 'v-profile' at x/D = 1.5 and retain a relatively symmetric profile. [9] documented a very similar wake behaviour measured by PIV. A significant difference between the flow at G/D = 0.6 and 1 is the recirculation area developed for the smaller gap. While relatively thin, it extends between x/D = 1.5 and 3 (see Figure 9a). As the gap becomes even smaller, the recirculation area becomes more prominent, covering a significantly longer and thicker layer. Time-averaged streamlines shown in Figure 10 give a confirmation of these zones, revealing that the one for G/D = 0.2 extends more than 6D downstream in

the wake. The downstream wall boundary layer is forced to separate because the streamlines in the inner shear layer become deflected away from the wall. [9] captured the recirculation only for a gap as narrow as 0.1D. Also measured by PIV, [8] reported such wall separation for $G/D \leq 0.6$, while LES results in [27] showed this behaviour for G/D = 0.25 and 0.5.

In Figure 9b, the present results are compared to the measurements of [8] for G/D = 0.2 and [9] for two comparable gaps, G/D = 0.1 and 0.3. [8] performed PIV measurements for Re = 9500, with the boundary layer thick enough to have the entire cylinder immersed in it (G/D = 1.4), comparable to the present simulations. Figure 9b shows very good agreement of the experimental and the present LES results in the near wake of the cylinder, confirming that the complex flow in the narrow gap between the cylinder and the wall is modelled correct. The discrepancies can first be noticed at x/D = 1, showing that LES yield a somewhat more upwards deflected wake.

[9] reported that such small G/D as 0.1 does not allow the development of the channelled flow below the cylinder. On the other hand, at G/D = 0.3, the velocity profile shows channelled flow farther downstream in the wake than for the present case. Qualitatively, the flow features are similar to the present study. The differences in the near wall flow might be attributed to a stronger interaction between the wall and the cylinder boundary layer for the smaller G/D = 0.2 in this study, as well as to the different $\delta/D$. Comparing their results to the previously published studies ([34] and [35]), [9] measured significantly smaller wake velocities. It is therefore important to have in mind the differences of the various experimental and numerical parameters, while recognizing the similar qualitative behaviour.

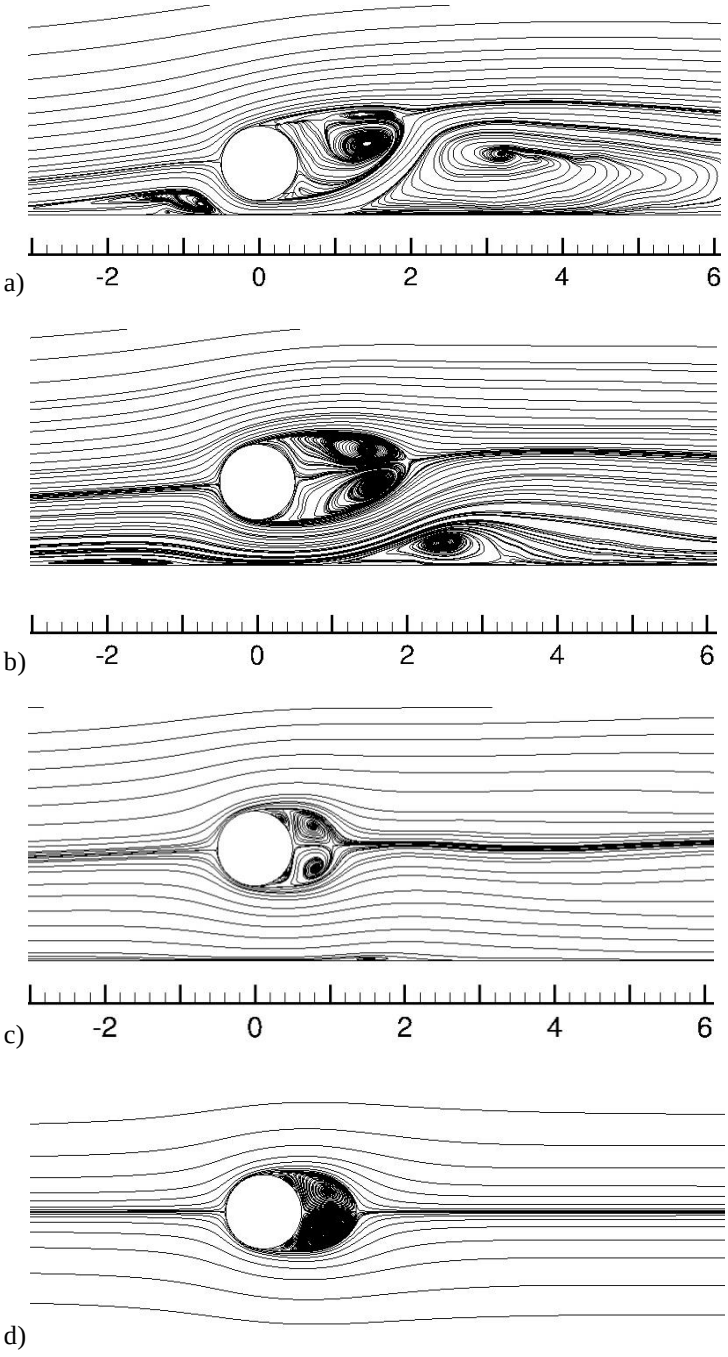


Figure 10. Time-averaged streamlines at z/D = 2 for G/D = 0.2, 0.6 and 1 at δ/D = 1.6. Cases a) G02 1, b) G06 1, c) G1 1 and d) cylinder in an infinite fluid (Re = 13100, Abrahamsen Prsic et al. [4]).

The distributions of the time-averaged streamlines for different G/D (Figure 10) show a clear distinction between the narrow and the wide gap regime. For G/D = 0.2 (Figure 10a), the flow behaves in the same manner as described by [27] and [30]. The flow upstream of the cylinder is characterized by a prominent separation region. Downstream, the flow accelerates between the wall and the cylinder. The coupling between the bottom boundary layer and the shear layer at the lower side of the cylinder causes the deflection of the primary bubble away from the wall. Similar to the observations by [27], Figure 10a shows the strong asymmetry between the vortices curling up from the upper and the lower

side of the cylinder. The whole primary bubble is relatively long and deflected upwards, leading to the formation of a large secondary bubble at the wall.

As the gap increases to G/D = 0.6 (Figure 10b), the upstream separation region reduces to a thin area. This shorter and flatter upstream region is also reported by [7]. The primary bubble, even though more symmetric, is still long and deflected from the wall. It allows the secondary recirculation to develop on the wall, but only in a small region in the near wake of the cylinder. The flow undergoes even more significant changes as the gap reaches G/D = 1 (Figure 10c), when the wall effect begins to cease. This is manifested through the disappearance of both the upstream and the downstream separation region, also reported by [27]. The primary separation bubble becomes symmetric and shortens to the size of the one behind a cylinder in an infinite fluid, also documented by [9]. Overall similarity of this wide gap flow and the flow around a cylinder in an unlimited fluid is shown in Figure 10c and 10d.

Through the experiments in the smoke tunnel, [10] photographed the flow behind the cylinder at G/D = 0.2 and 1.2, at Re = 45000 (Figure 11a and 11b). The photographs are compared to the instantaneous streamlines at the cylinder mid-section for the cases G/D = 0.2 and 1 (Figure 11c and 11d). This comparison gives an example that the experimental and the numerical results are complementary. While the experimental results offer a clear and trustworthy overview of the dynamic flow phenomena, the nature of the smoke tunnel experiments does not allow capturing the fine structures in the cylinder wake. On the other hand, while agreeing with the experiments, LES also provide a unique detailed insight in the fine structures in the cylinder wake.

At G/D = 0.2, both the experimental and the numerical results show that the vortices in the near wake are restricted to the upwards deflected separation bubble. The length of the primary bubble as well as the position of the secondary bubble from this study compare well with [10], see Figure 11a and 11c. The similarity of the instantaneous and the time-averaged streamlines (Figure 10a and 11c) confirms that there are only slight variations of the wake with time. On the other hand, G/D = 1 and 1.2 allow for the vortex street to develop, as captured both by the experiments and the LES. Figures 11b and 11d show clear similarity, with comparable size and shape of the vortices in the cylinder wake.

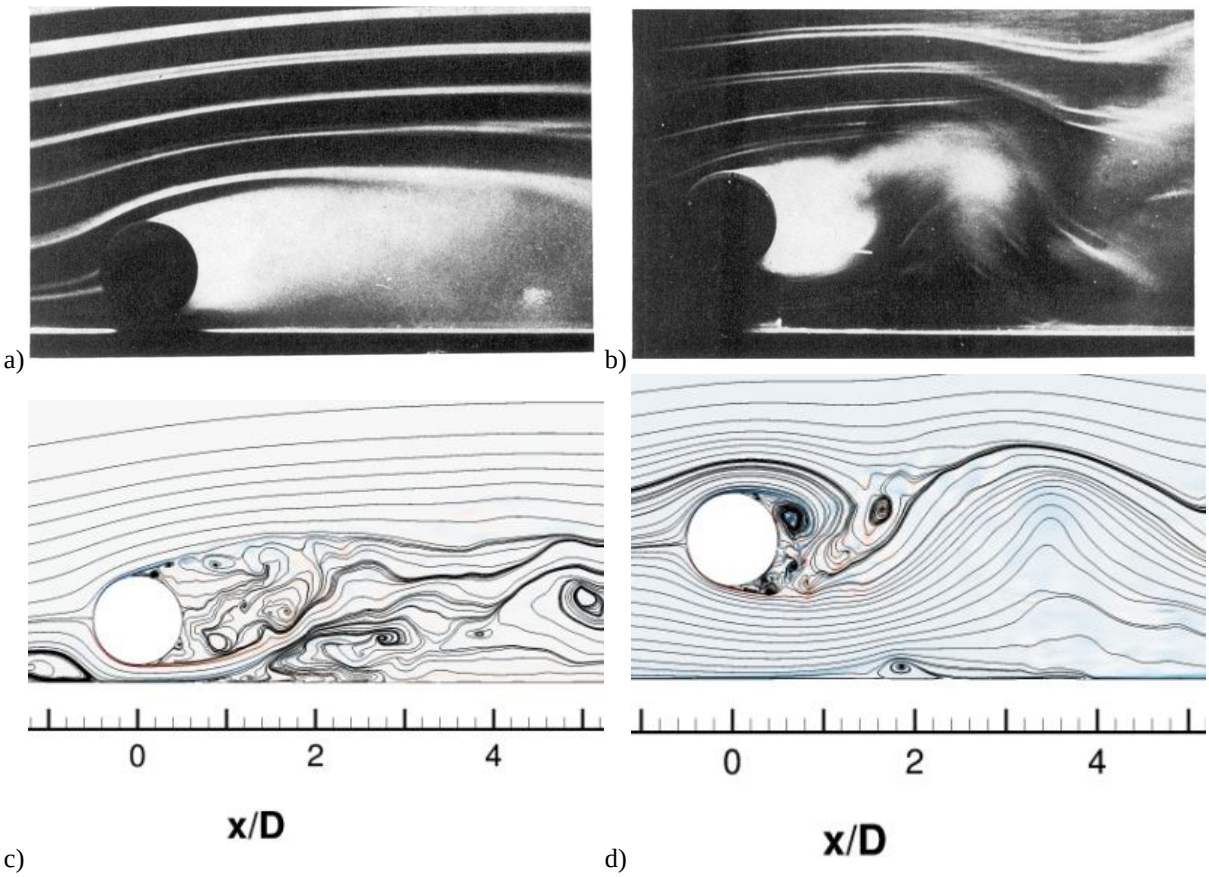


Figure 11. Instantaneous flow pattern. Figures 11a and 11b are taken from Bearman and Zdravkovich [10]. The wind tunnel measurements are performed for Re = 2.5 x $10^4$.

a) G/D = 0.2.
b) G/D = 1.2.
c) G/D = 0.2. Present study, case G02 1.
d) G/D = 1. Present study, case G1 1.

The instantaneous streamlines presented in 11c and 11d are taken at cylinder mid-plane, z/D = 2 for Re = 1.31 x $10^4$ and $\delta/D = 1.6$.

The instantaneous Q = 1 iso-surfaces offer an insight into the development of the three-dimensional vortex structures in the cylinder wake. The inhibition of the vortex shedding for G/D = 0.2 is clearly shown in Figure 12a. The upper shear layer extends relatively far into the wake, while the lower shear layer deflects from the wall. The resulting long separation region is also detectable in Figure 12a. In the cylinder wake, no signs of large coherent structures are observed; the small scale eddies dominate the wake flow. The wall separation region is also present.

As the gap increases, the von Karman vortex street, dappled with smaller eddies, is observed in Figures 12b and 12c. The upper shear layers become shorter. For the large gap, the shear layers shed and curl up on both sides of the cylinder, creating a regular vortex shedding pattern. However, at G/D = 0.6, the lower part of the cylinder is affected by the gradients in the wall boundary layer. In agreement with [13], the boundary layer interacts with the vortices shed from the lower half of the cylinder. They travel downstream at lower speed, experiencing more damping than the ones shed from the upper half of the cylinder. While deformation of the vortices in the vicinity of the wall is also

noticeable for the largest gap (Figure 12c), stronger symmetry and coherence indicate a significant weakening of the wall influence.

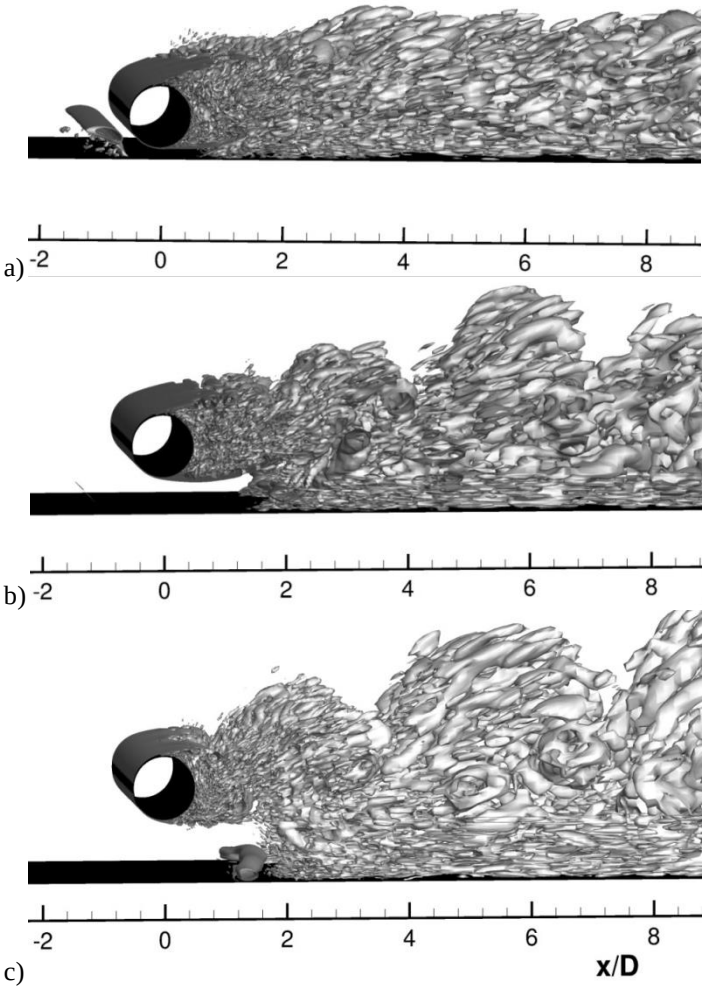


Figure 12. Instantaneous Q = 1 iso-surfaces for G/D = 0.2, 0.6 and 1. Cases a) G02 1, b) G06 1 and c) G1 1 at δ/D = 1.6. The spanwise length of the cylinder is 4D.

The suppression of the vortex shedding is analysed through the energy spectra sampled in the near wake of the cylinder for G/D = 0.2, 0.6 and 1 (Figure 13). G/D = 1 allows the vortex shedding to fully develop, resulting in a single, prominent peak of the energy spectrum, corresponding to St. For G/D = 0.6, the energy spectrum has maximum at a frequency slightly higher than for G/D = 1 and for a cylinder in infinite fluid [4], [15]. The maximum is, however, less prominent, confirming the previous conclusion about the attenuation of the vortex shedding. The complete absence of the regular von Karman vortex street for G/D = 0.2 is confirmed in Figure 13.

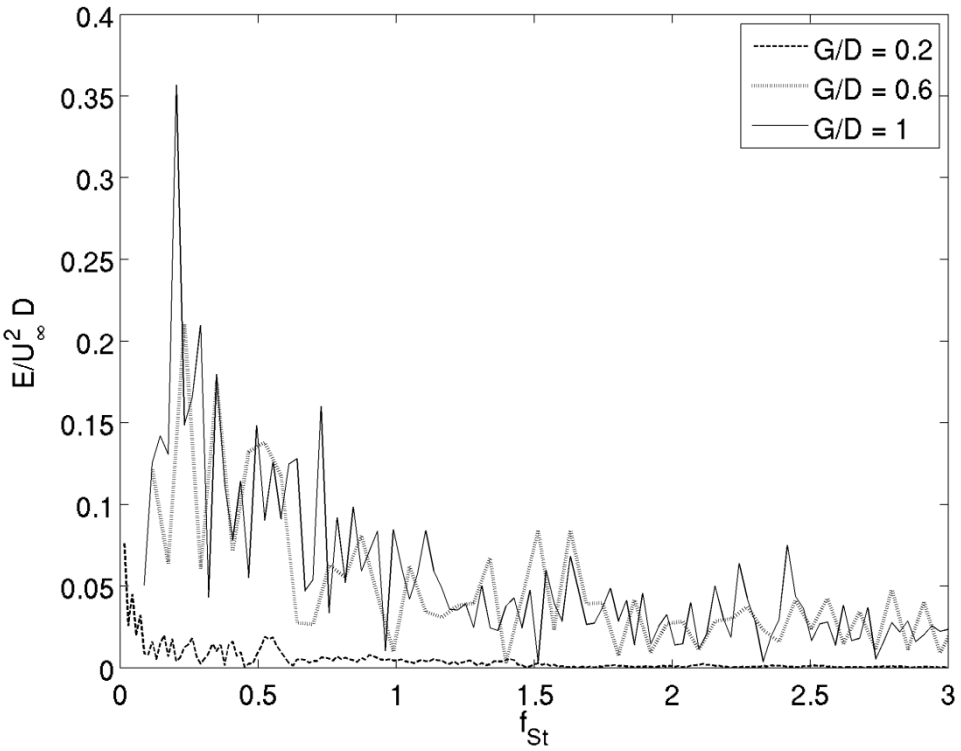


Figure 13. Energy spectra in the cylinder wake, sampled at x/D = 1, y/D = 0.3, z/D = 0. The normalized Strouhal frequency is given as $f_{St} = f^*D/U_c$.

## 4.2. Influence of incoming boundary layer thickness δ/D

The flow dependency on the thickness of the incoming boundary layer profile is examined through three simulations with constant G/D = 0.6, and varying δ/D (see Table 3). The logarithmic profile is chosen to simulate a developed boundary layer profile near a flat, rigid wall.

Contrary to the extensive number of studies investigating the influence of G/D, data available on the influence of δ/D is scarce. [31] conducted a series of experiments for a higher Re varying between 48000 and 140000. This Re range is, however, in the same flow-regime as the present study. The analysis was focused on the gap to boundary layer thickness ratio, G/δ, showing that $\overline{C_d}$ decreases as G/δ decreases below 1 and maintains a slowly increasing trend for G/δ > 1. For Re = 61000, [31] obtained $\overline{C_d}$ = 0.64, 0.96 and 1.05 for δ/D = 0.4, 1.2 and 2, respectively. While the present $\overline{C_d}$ values are higher for all δ/D, the same trend is observed (Figure 14a). The present values are in better agreement with the experimental study by [11] at a closer Re = 13000, as shown in Figure 14a.

$C_{lrms}$ also decreases with increasing boundary layer thickness (Figure 14b). For the thinnest boundary layer, both $\overline{C_d}$ and $C_{lrms}$ behave comparable to the cylinder in an infinite fluid. As the boundary layer thickens, the gap and the cylinder itself get immersed into the bottom boundary layer,

leading to lower $C_{lrms}$. [11] and [31] report a similar trend for the $C_{lrms}$, showing a prominent decrease as the cylinder becomes immersed in the boundary layer.

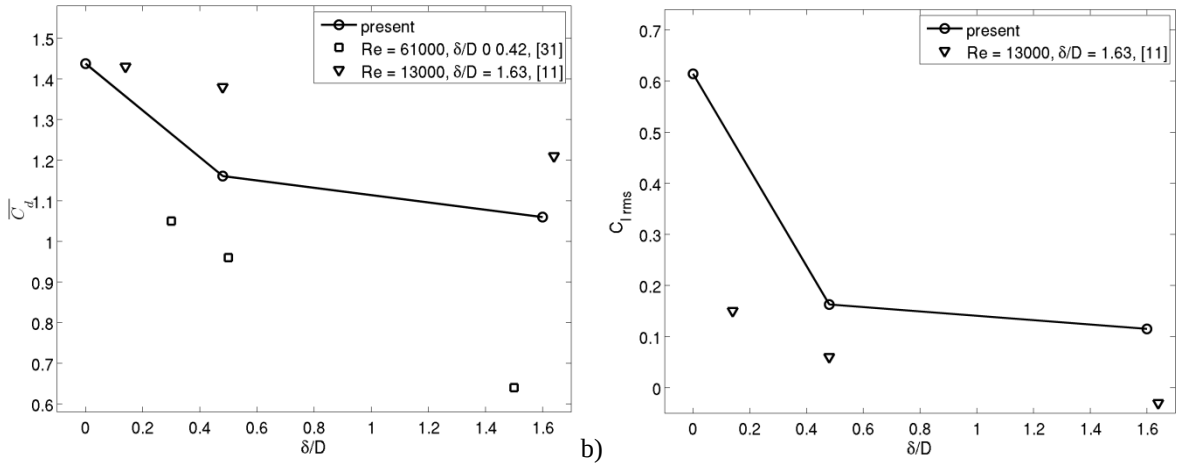


a) b)

Figure 14: $\overline{C_d}$ and $C_{l\,rms}$ versus δ/D for G/D = 0.6.

The mean pressure coefficient ($\overline{C_p}$) distribution is analysed in Figure 15; $\overline{C_p}$ is the time- and spanwise-averaged pressure coefficient, and $C_p = (p'-p_\infty)/(0.5\rho U_c^2)$, for the fully developed flow. Here p' is the instantaneous pressure at the sampling point, and $p_\infty$ is the pressure in the undisturbed flow. Here θ = 0 corresponds to the point at the cylinder closest to the wall and θ increases clockwise (see Figure 1).

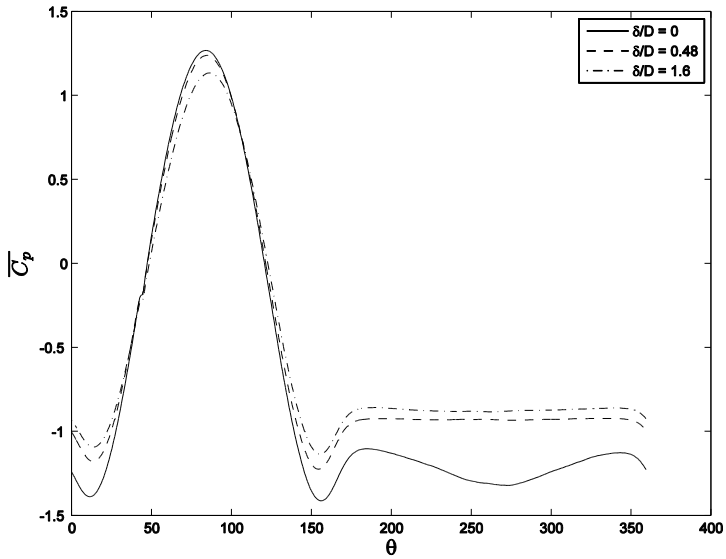


Figure 15. $C_p$ distribution versus δ/D ratio for G/D = 0.6. The angle θ is defined in Figure 1.

A thinner boundary layer leads to a more pronounced maximum in $\overline{C_p}$. This behaviour is also reported by [11], who connected it to the exposure of the gap to the velocity gradient in the boundary layer. Exposure to the gradient can also be obtained by decreasing G/D, causing a similar effect. The

decrease of the $\overline{C_p}$ peak with a reduced gap is documented by [12] and [23]. The thickening of the wall boundary layer causes an increase of the base pressure. In the entire $\overline{C_p}$ profile, Figure 15 shows the largest increase from the thinnest (δ/D = 0) to the intermediate (δ/D = 0.48) boundary layer, while further thickening of δ/D results in smaller increase of the magnitude.

Mean velocity profiles in the cylinder wake are presented in Figure 16a. In the near wake (x/D = 0 to 1), all three cases with different boundary layers exhibit similar profiles. Farther downstream, the two cases with thicker boundary layers behave similarly, maintaining a significant profile curvature up to x/D = 3. The thinnest boundary layer results in symmetric, but earlier flattened wake profile, indicating a shorter wake. The present results are compared with the PIV measurements, [9], for the same G/D = 0.6, comparable δ/D = 0.4 and Re = 12000. The qualitative behaviour of the profiles is similar, exhibiting the symmetry, the relatively late flattening of the profiles, and the transition from the characteristic 'u-' to 'v-profile'. However, all measurements for the various cases presented by [9] result in smaller velocities compared to the previously published and the present results. The focus is therefore on the qualitative comparison.

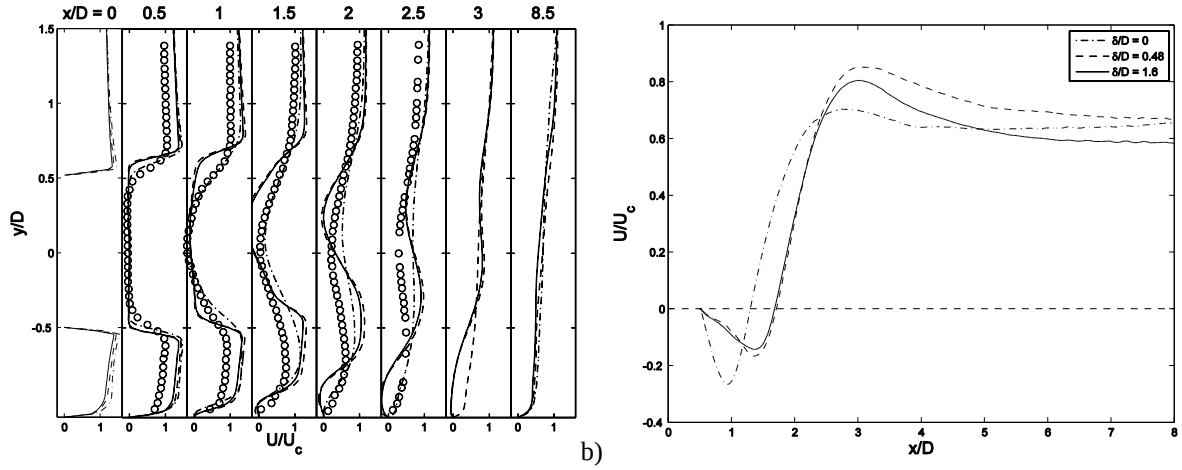


a) b)

Figure 16. Mean, normalized streamwise velocity component ($U/U_c$) in the cylinder wake, G/D = 0.6

a) in the (y, z) plane. Present study and "o" δ/D = 0.4, Re = 1.2 x $10^4$, Wang and Tan [9];
b) in the (x, z) plane, y/D = 0 versus the δ/D, present study.

The analogy between the reduced thickness of the boundary layer and the widening of the gap can also be noticed in Figure 16b. While the near wakes for the two thicker boundary layers exhibit longer recirculation lengths and somewhat higher velocities, the wake profile of the thinnest boundary layer shows more resemblance with the one of the cylinder at large G/D. Comparison of the time-averaged streamlines for these three δ/D cases at G/D = 0.6 (Figure 17) with the wide gap, G/D = 1 (Figure 10c) and the cylinder in the infinite fluid (Figure 10d) further confirms this. For δ/D = 0 (Figure 17a), the upstream separation region vanishes while the downstream region is reduced. However, the presence of the wall still causes the deflection of the wake away from the wall, for G/D

= 0.6. The thicker boundary layers engulf the channel between the cylinder and the wall, allowing the fluid particles to accelerate and eventually cause the upturn of the boundary layer. This results in longer primary bubbles and the prominent downstream separation zones for both δ/D = 0.48 (Figure 17b) and δ/D = 1.6 (Figure 17c).

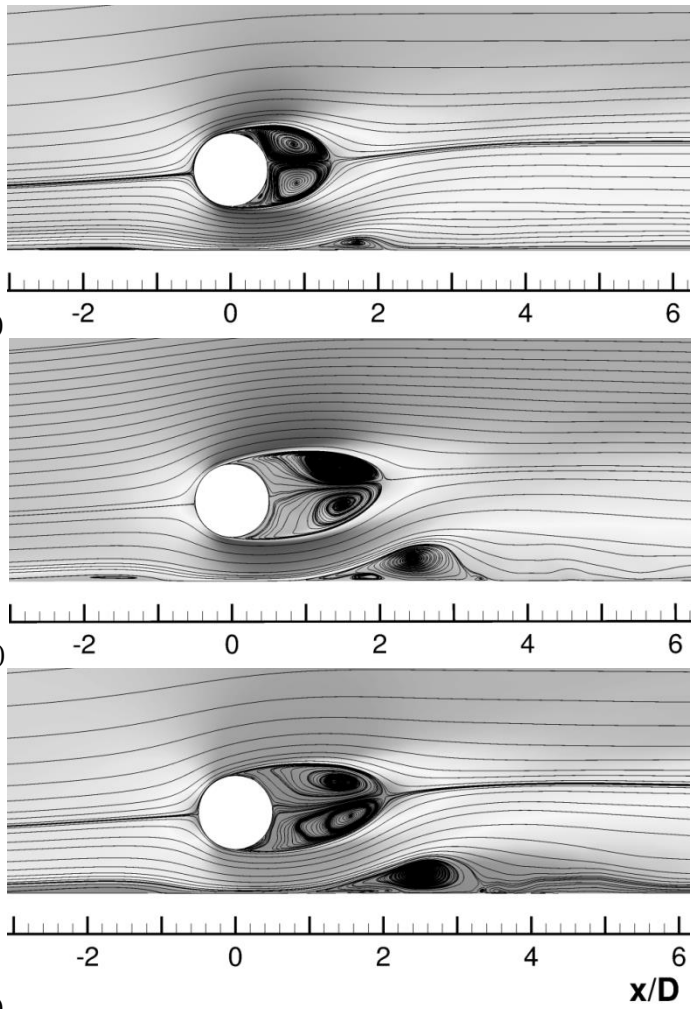


Figure 17. Time-averaged streamlines and $U/U_c$ at z/D = 2. δ/D = 0, 0.48 and 1.6, G/D = 0.6 in all cases.

## *5. Conclusions*

Near-wall flow effects on a circular subsea pipeline in the vicinity of the seabed at Re = 13100 are investigated by LES with Smagorinsky sub-grid scale model. The effects of the distance between the cylinder and the seabed, and the bottom boundary layer thickness, on the forces exerted on the cylinder and the flow field in the cylinder wake, are presented. The main conclusions are:

The gap to diameter ratio, G/D, has a strong influence on the forces on the cylinder and the development of the flow in the wake. For G/D smaller than the critical gap, the vortex shedding is suppressed, noticed in the present study for G/D = 0.2. Increasing G/D, asymmetric vortex shedding develops (demonstrated for G/D = 0.6). Due to the reduced interaction between the wall and the cylinder boundary layer for the larger G/D = 1, the wake flow approaches the behaviour of a cylinder in an infinite fluid and uniform incoming velocity field.

By varying G/D, different aspects of the flow are displayed:

a) For G/D = 0.2, both the primary and the secondary separation bubble are long and nearly stationary.

b) The intermediate G/D = 0.6 yields a slightly asymmetric wake, with long shear layers. The vortex shedding is limited and the secondary circulation at the wall boundary layer is substantial.

c) The large G/D = 1 allows a symmetric near wake (with respect to x-axis), while eddies interact with the wall farther in the wake. The cylinder shear layers and the wall boundary layer separate periodically.

Although the presence of the plane wall has the strongest influence on the general flow characteristics, it also depends on the boundary layer thickness to diameter ratio, $\delta/D$, and the shape of the boundary layer. Effects of a thicker boundary layer are similar to the effects of decreasing G/D. For G/D = 0.6, if the cylinder is not immersed in the boundary layer, the flow resembles the one around the cylinder in an infinite fluid. Larger $\delta/D$, where the cylinder is subjected to the shear flow, results in lower $\overline{C_d}$ and $C_{lrms}$, as well as an elongated and asymmetric wake.

Comparison of the present results with the experimental measurements shows that LES are a good numerical tool for the actual flow case. The 3D simulations also complement the experiments, offering insight into the detailed structures in the cylinder wake and allowing thorough exploration of the three-dimensional flow behaviour. 3D LES offer clear improvements compared to the commonly used simple 2D RANS models as well as to 2D LES, giving more reliable integrated forces and capturing the details of the flow at different G/D and $\delta/D$, important for the structural analysis of the pipeline.

## *Acknowledgements*

This work has been supported by the Norwegian University of Science and Technology (NTNU). Computing time on the supercomputer 'Vilje', supported by NOTUR (the Norwegian Metacenter for Computational Science) is granted by the Norwegian Research Council and NTNU. This support is gratefully acknowledged.

# *References*


[1] Breuer, M., 1998. Large eddy simulation of the subcritical flow past a circular cylinder: numerical and modeling aspects. International Journal for Numerical Methods in Fluids, 28, 1280-1302.

[2] Tremblay, F., Manhart, M., Friedrich, R., 2000. DNS of flow around the circular cylinder at subcritical Reynolds number with Cartesian grids. Proceedings of the 8th European Turbulence Conference, EUROMECH, Barcelona, Spain, 659-662.

[3] Parnaudeau, P., Carlier, J., Heitz, D., Lamballais, E., 2008. Experimental and numerical studies of the flow over a circular cylinder at Reynolds number 3900. Phys. Fluids 20, 085101.

[4] Abrahamsen Prsic, M., Ong, M. C., Pettersen, B., Myrhaug D., 2014. Large-eddy simulations of three dimensional flow around a smooth circular cylinder in a uniform current in the subcritical flow regime. Ocean Engineering, 77, 61-73.

[5] Knight, P. J., Wilkinson, M., Glorioso, P., 1993. Current profile and sea-bed pressure and temperature records from the northern North Sea. Challenger Cruises 84 and 85. September 1991 - November 1991. Birkenhead, Proudman Oceanographic Laboratory, 417pp. Proudman Oceanographic Laboratory, Report No. 28.

[6] Offshore standard Det Norske Veritas as Dnv-Os-F101; Submarine pipeline systems. Det Norske Veritas, August 2012.

[7] Price, S. J., Sumner, D., Smith, J. G., Leong., K., Paidoussis, M. P., 2002. Flow visualization around a circular cylinder near to a plane wall. Journal of Fluids and Structures, 16(2), 175-191.

[8] Alper Oner, A., Salih Kirgoz, M., Sami Akoz, M., 2008. Interaction of a current with a circular cylinder near a rigid bed. Ocean Engineering, 35, 1492-1504.

[9] Wang, X. K., Tan, S. K., 2008. Comparison of flow patterns in the near wake of a circular cylinder and a square cylinder placed near a plane wall. Ocean Engineering, 35, 458-472.

[10] Bearman, P. W., Zdravkovich, M. M., 1978. Flow around a circular cylinder near a plane boundary. Journal of Fluid Mechanics, 89, 33-47.

[11] Lei, C., Cheng, L., Kavanagh, K., 1999. Re-examination of the effect of a plane boundary on force and vortex shedding of a circular cylinder. Journal of Wind Engineering and Industrial Aerodynamics, 80, 263-286.

[12] Han, Y., Shi, B., Ren, X., Jing, X., 2009. Experimental study on the distribution of velocity and pressure near a submarine pipeline. J. Ocean Univ. China (Oceanic and Coastal Sea Research), 8(4), 404-408.

[13] Brørs, B., 1999. Numerical modelling of flow and scour at pipelines. Journal of Hydraulic Engineering, 125 (5), 511-523.

[14] Ong, M. C. ,Utnes, T., Holmedal, L. E., Myrhaug, D., Pettersen, B., 2010. Numerical simulation of flow around a circular cylinder close to a flat seabed at high Reynolds numbers using a k- ε model. Coastal Engineering, 57 (10), 931-947.

[15] Lysenko, D. A., Ertesvåg, I. E., Rian, K. E,, 2012. Large-eddy simulation of the flow over a circular cylinder at Reynolds number 3900 using the OpenFOAM toolbox. Flow Turbulence Combust. 89, 491-518.

[16] Liou, T.-M., Chen, S.-H., Hwang, P-W., 2002. Large eddy simulation of turbulent wake behind a square cylinder with nearby wall. Journal of Fluids Engineering, 124, 81-90.

[17] Boileau, M., Duchaine, F., Jouhaud, J.-C., 2013. Large-Eddy Simulation of heat transfer around a square cylinder using unstructured grids. AIAA Journal. 51 (2), 372-385.

[18] Smagorinsky, J., 1963. General circulation experiments with the primitive equations. Monthly Weather Review, 91 (3), 99-164.

[19] Breuer, M., 2000. A challenging case for large eddy simulation of high Reynolds number circular cylinder flow. International Journal of Heat and Fluid Flow, 21, 648-654.

[20] Ferziger, J. H., Peric, M., 2002. Computational methods for fluid dynamics. 3rd Ed, Springer-Verlag, Berlin, Germany.

[21] Krajnovic, S., 2011. Flow around a tall finite cylinder explored by large eddy simulation. Journal of Fluid Mechanics 676, 294–317.

[22] Liang, D., Cheng, L., 2005. Numerical modeling of flow and scour below a pipeline in currents; Part 1. Flow simulation. Coastal Engineering, 52, 25-42.

[23] Ong, M. C., Utnes, T., Holmedal, L. E., Myrhaug, D., Pettersen, B., 2012. Near-bed flow mechanisms around a circular marine pipeline close to a flat seabed in the subcritical flow regime using a k - ε model. Journal of Offshore Mechanics and Arctic Engineering, 134 (2), 021803.

[24] ASME V&V 20, 2009. Standard for Verification and Validation in Computational Fluid Dynamics and Heat Transfer. ASME, New York, USA.

[25] Sumer, B. M., Fredsøe, J., 2010. Hydrodynamics Around Cylindrical Structures, Revised Edition. Advanced Series on Ocean Engineering, World Scientific Publishing, Singapore.

[26] Novak, M., Tanaka, H., 1977. Pressure correlations on a vibrating cylinder. Proc. 4th Int. Conference on Wind Effects on Buildings and Structures, Heathrow, UK., Ed. By Eaton., K. J. Cambridge University Press, pp. 227-232.
[27] Sarkar, S., Sarkar, S., 2010. Vortex dynamics of a cylinder wake in proximity to a wall. Journal of Fluids and Structures, 26, 19-40.
[28] Wissink, J. G., Rodi, W., 2008. Large-scale computations of flow around a circular cylinder; in Resch, M., Roller, S., Lammers, P., Furui, T., Galle, M., Bez, W. 2008. High Performance Computing on Vector Systems. Springer-Verlag, Berlin Heidelberg, Germany.
[29] Lesieur, M., Metais, O., Comte, P., 2005. Large-Eddy Simulations of Turbulence. Cambridge University Press, New York, USA.
[30] Zdravkovich , M. M., 2009. Flow around circular cylinders. Vol.2: Applications. Oxford University Press, Oxford, United Kingdom.
[31] Zdravkovich, M. M., 1985. Forces on a circular cylinder near a plane wall. Applied Ocean Research, 7 (4), 197-201.
[32] Zhao, M., Cheng, L., Teng, B., 2007. Numerical modeling of flow and hydrodynamic forces around a piggyback pipeline near the seabed. Journal of Waterway, Port, Coastal and Ocean Engineering, v 133, n 4, p 286-295.
[33] Zdravkovich, M. M. 1997. Flow around Circular Cylinders: Vol 1: Fundamentals. Oxford University Press, Oxford, United Kingdom.
[34] Bosch, G.,Rodi, W., 1996. Simulation of vortex shedding past a square cylinder near a wall. International Journal of Heat and Fluid Flow, 17 (3), 267-275.
[35] Bo, J. C, Hui, D. L., Fang, L. D., 2003. Study of concentration fields in turbulent wake regions. Journal of Hydraulic Research, 41 (3), 311-318.